Energy, Environmental, and Catalysis Applications

Macroscale and Nanoscale Photoelectrochemical Behavior of p-Type Si(111) Covered by a Single Layer of Graphene or Hexagonal Boron Nitride

Annelise Christine Thompson, Burton H. Simpson, and Nathan S. Lewis

ACS Appl. Mater. Interfaces, **Just Accepted Manuscript** • DOI: 10.1021/acsami.9b21134 • Publication Date (Web): 10 Feb 2020

Macroscale and Nanoscale Photoelectrochemical Behavior of p-Type Si(111) Covered by a Single Layer of Graphene or Hexagonal Boron Nitride

Annelise C. Thompson‡, Burton H. Simpson‡, and Nathan S. Lewis.*

Division of Chemistry and Chemical Engineering, California Institute of Technology, Pasadena, CA, 91125, United States

KEYWORDS: 2D material, graphene, hexagonal boron nitride, photoelectrochemistry, semiconductor/liquid junction, scanning electrochemical cell microscopy

ABSTRACT: Two-dimensional (2D) materials may enable a general approach to introduction of a dipole at a semiconductor surface as well as control over other properties of the double layer at a semiconductor/liquid interface. Vastly different properties can be found in the 2D materials currently studied due in part to the range of the distribution of density-of-states. In this work, the open-circuit voltage (V_{oc}) of p-Si–H, p-Si/Gr (graphene) and p-Si/h-BN (hexagonal boron nitride) in contact with a series of one-electron outer-sphere redox couples was investigated by macroscale measurements as well as by scanning electrochemical cell microscopy (SECCM). The band gaps of Gr and h-BN (0-5.97 eV) encompass the wide range of band gaps for 2D materials, so these interfaces (p-Si/Gr and p-Si/h-BN) serve as useful references to understand the behavior of 2D

materials more generally. The value of V_{oc} shifted with respect to the effective potential of the contacting solution, with slopes ($\Delta V_{oc}/\Delta E_{Eff}$) of -0.27 and -0.38 for p-Si/Gr and p-Si/h-BN respectively, indicating that band bending at the p-Si/h-BN and p-Si/Gr interfaces responds at least partially to changes in the electrochemical potential of the contacting liquid electrolyte. Additionally, SECCM is shown to be an effective method to interrogate the nanoscale photoelectrochemical behavior of an interface, showing little spatial variance over scales exceeding the grain size of the CVD-grown 2D materials in this work. The measurements demonstrated that the polycrystalline nature of the 2D materials had little effect on the results and confirmed that the macroscale measurements reflected the junction behavior at the nanoscale.

Introduction

Covalent functionalization of semiconductor surfaces is an established method for manipulating the energetics of semiconductor interfaces. Development of the chemistry needed for such functionalization can be time-consuming, and this strategy is not easily translated between materials without extensive work to develop and characterize new reactions. Coating semiconductors such as n-type silicon (n-Si) with a monolayer of graphene (Gr) or fluorinated graphene (F–Gr) represents a potentially general strategy for protection of semiconductor surfaces against oxidation during photoanodic operation in aqueous solution as well as for manipulation of the band-edge positions and energetics of the semiconductor/liquid interface.[1-2] The open-circuit voltage (V_{oc}) of these electrodes shifts in contact with a series of nonaqueous redox couples of varying potentials, indicating a lack of Fermi-level pinning even though the Fermi level (E_F) of monolayer Gr is similar to that of graphite (-4.6 eV vs. vacuum), and lies mid-gap relative to the silicon band-edge positions.[3] With the recent expansion of the number

and classes of two-dimensional (2D) materials that can be isolated, covering semiconductors with 2D materials may represent an effective method to manipulate, as determined by the electronic states in the 2D material, the interfacial energetics and chemistry of semiconductor surfaces.

Further understanding the effects of the density of states of a 2D material on an interface is key to the successful integration of these materials into devices. Many of the extraordinary properties that have made Gr so well studied arise from the existence of a Dirac point in the density of states.[4] The electronic structure of Gr also results in the presence of a finite number of surface states within the band gap of silicon. These states contribute to the formation of a rectifying potential-dependent barrier height (φ_B) in contact with both n-type and p-type Si, unlike the potential-independent barrier heights of many semiconductor-electrolyte and semiconductor-metal interfaces[5]. However, these states, and the resulting dependence of the barrier height on potential, can also attenuate the barrier height of fabricated devices by partially or fully pinning the interface energetics.[1, 6-7] In contrast, hexagonal boron nitride (h-BN), a structural analogue of Gr consisting of an alternating lattice of boron and nitrogen atoms, is primarily used as an inert protective layer in 2D material heterostructures. h-BN is an insulator with a band gap of 5.97 eV.[8] Gr has found widespread application in photoelectrochemical cells, including as a transparent electrode and catalyst support,[9] while h-BN has been demonstrated to be an effective tunnel barrier even at a monolayer[10] and enhances the performance of Gr-on-Si Schottky junction solar cells.[11] h-BN should not introduce states within the band gap of Si and thus should provide a useful endpoint for comparison with Gr, because the band gaps of most 2D materials fall between the range presented by these two materials (0 eV-5.97 eV). Moreover, the behavior of each at an interface should be reflective of the density of states within the band gap of Si.

Substantial discrepancies have been reported between barrier heights of Si/2D/metal interfaces. An ohmic contact has been observed for an n-Si/Gr/Ni junction using nanoscale AFM measurements (contact size diameter ~ 40-50 nm),[12] whereas macroscale measurements (contact size diameter ~ 500 μm) of the same interface have been reported to exhibit strongly rectifying behavior.[7] Additional work has shown that the φ_B of an n-Si/2D/metal interface is fully pinned with respect to the work function of metal, across a range of contact sizes (60 nm-100 μm).[6] Both the size of the metal contact and the measurement technique have an effect on the observed behavior of Si/2D/metal interfaces. In these Si/2D/metal interfaces, simulations have indicated that the distance between the 2D material and metal top contact, and hybridization of that metal with the 2D material in question through physisorption or chemisorption, decrease the resulting φ_B of the interface.[13-14] This hybridization causes an analogous, but fully 2D material heterojunction formed from MoS_2/Gr/metal to exhibit lower contact resistances when a purposefully defective Gr layer is inserted at the interface, allowing increased interactions between the Gr and metal.[15] This variance in observed behavior at Si/2D/metal interfaces, and the dependence of contact resistance on defects, collectively complicate formulation of a complete understanding electron-transfer at the interface especially as more complex stacks are constructed. Techniques that rely on formation of metallic top contacts do not readily facilitate resolution of differences in spatial heterogeneity across an interface nor provide results that are readily compared with macroscale measurements. Thus, to systematically understand how the properties of the semiconductor/2D interface vary, devices with uniform, nondestructive top contacts, such those formed in a liquid junction cell, can be used to avoid the substantial effect of the 2D material/metal interaction on the semiconductor/2D/contact interface. An understanding of the role of Gr and h-BN at a semiconductor/liquid junction, which affords precise control over the potential of the interface,

will inform further work on the trends expected from more complex semiconductor/stacked 2D material heterojunctions.

Ideal interfaces could be produced using exclusively pristine, single crystals of the 2D material, but such samples are technologically not yet available for measurements on macroscale electrodes. Single crystals of 2D materials can be obtained through mechanical exfoliation of layered materials, but these methods do not produce single crystals of a size large enough to cover even laboratory-scale (~1 cm^2) photoelectrodes. Consequently, in our work, 2D materials grown by chemical-vapor deposition (CVD) have been used to produce large (>1 cm^2) area samples. CVD-grown 2D materials currently represent the materials most similar to those easily used in both general research and industrial device fabrication. However, CVD-grown Gr and h-BN are both polycrystalline materials that inherently contain grain boundaries and defects. The distinct differences between the electronic structure of the pristine material and the defective sites may locally impact the energetics at the semiconductor/2D/liquid junction and thus also influence the macroscale behavior of such systems.[16] To address this issue, scanning electrochemical cell microscopy (SECCM) has been used herein to supplement macroscale understanding of the junction energetics with submicron spatial resolution, which is a length scale sufficient to interrogate the behavior within a grain of the CVD-grown 2D materials studied in our work.

SECCM is a scanning probe microscopy technique introduced by Unwin in 2010 that utilizes an electrolyte-filled glass nanopipette as the probe.[17] The counter and reference electrodes of an electrochemical cell are housed within this pipette and connected to a potentiostat. Using a micropositioner, the opening of the pipette is brought close to a surface being operated as the working electrode, until a nanoscale liquid junction is formed between the pipette and the surface, completing the circuit for the electrochemical cell. The probe is then operated as an

electrochemical cell with a working electrode area defined by the size of the liquid junction. SECCM allows standard electrochemical techniques to be performed with a high degree of spatial resolution,[18-19] and has previously been used in photoelectrochemical systems to measure and resolve photocurrents on heterogeneous surfaces.[20] In addition to enabling spatially resolved electrochemistry, the small surface area of the working electrode in contact with electrolyte makes SECCM especially useful for samples that may readily degrade or change structure under electrochemical operation, because a location can be tested without affecting the remainder of the sample.

Scanning electrochemical microscopy (SECM) and SECCM have previously revealed differences between the macroscale and nanoscale electrochemistry of 2D materials. CVD-grown Gr often exhibits lower interfacial electron-transfer rate constants than graphite, the bulk equivalent of Gr. SECM studies using nanoelectrodes have indicated that this difference is specific to Gr electrodes that are supported by polymethyl methacrylate (PMMA), as is commonly practiced in fabrication of Gr devices.[21] In contrast, polystyrene-supported electrodes had electron-transfer rates that were similar to those of graphite. These techniques have also been used to probe heterogeneity in electrochemical reactivity across the surfaces of 2D materials. Gr edges at mechanically induced defects exhibit interfacial electron-transfer rate constants nearly an order of magnitude higher than rate constants measured for the Gr basal plane.[22] Notably, the spatial resolution of the electrodes used in that study would result in contributions to the observed kinetics from both basal plane and edge sites. SECCM studies have probed the impact of the number of Gr layers on the electrochemical kinetics, and concluded that the reactivity is largely determined by the density of states, with exposed edges showing especially high reactivity.[19] Similarly increased activity has

been observed at the edges of exfoliated MoS_2 nanoflakes using scanning photocurrent microscopy.[23]

For a complete understanding of 2D material/semiconductor interfaces, the effect of the density-of-states of a 2D material on the resulting junction must be systematically understood. We have used macroscale photoelectrochemical measurements to probe the effect of 2D materials that have substantially different mutual distributions of their density-of-states by comparing the photoelectrochemical behavior of Gr and h-BN covered p-type silicon (p-Si) photoelectrodes to H-terminated p-Si (111) surfaces. Inserting two-dimensional materials at the semiconductor/liquid junction are shown to have a measurable impact on junction energetics through the equilibration of the Fermi levels of the semiconductor and the 2D material, depending on the density of states of the interstitial 2D material. Supporting measurements on the nanoscale with SECCM probes that are far smaller than the grain size of the 2D materials used in this study corroborates the trends of the p-Si/2D junctions recorded on the macroscale without substantial contributions from grain boundaries. By establishing the macroscale behavior of conductive and insulating 2D materials as interstitial layers and developing liquid probes to interrogate junction energetics on the macroscale, this study develops the fundamental understanding needed to successfully integrate 2D materials into photoelectrochemical devices.

Methods

Materials

Acetonitrile (Dri-Solv, 99.9%) was purchased from Fisher Scientific and used as received. Lithium perchlorate ($LiClO_4$, 99.99%, battery grade) was purchased from Sigma Aldrich and used as received.

Ferrocene (Cp_2Fe^0), dimethylferrocene ($Me_2Cp_2Fe^0$), decamethylferrocene ($Cp^*_2Fe^0$) nickelocene (Cp_2Ni^0), and cobaltocene (Cp_2Co^0) were all purchased from Sigma-Aldrich and purified by sublimation. Octamethylnickelocene ($Me_8Cp_2Ni^0$) was purchased from Sigma-Aldrich and used as received. Cobaltocenium (Cp_2Co^+) hexafluorophosphate (Sigma-Aldrich, 98%) was recrystallized from ethanol. Decamethylcobaltocenium ($Cp^*_2Co^+$) hexafluorophosphate (Sigma-Aldrich, 98%) was recrystallized from CH_3CN using ethanol as an antisolvent. Methyl viologen hexafluorophosphate ($MV(PF_6)_2$) was prepared by metathesis of methyl viologen dichloride (Sigma-Aldrich, 98%) with ammonium hexafluorophosphate (Sigma-Aldrich, 99.98%) in water, and was recrystallized from ethanol.

All chemicals were stored in a $N_2(g)$-filled flush box that contained <3 ppm $O_2(g)$. Electrolyte solutions were prepared in the flush box using CH_3CN with 0.50 M $LiClO_4$ as the supporting electrolyte. Except for $Cp^*_2Fe^0$ and MV^{2+}, which had limited solubility, all of the redox couples were prepared at initial concentrations of ~10 mM of the available species. Bulk electrolysis was used to generate the reduced species Me_8Cp_2Ni, $MV^{+\cdot}$, and Cp^*_2Co, as well as all of the oxidized forms of the metallocenes except Cp_2Co^+.

For electrochemical measurements, double-side polished, boron-doped, p-type Si(111) wafers (0.3 Ω cm resistivity, with an acceptor concentration, $N_A = 7 \times 10^{16}$ cm^{-3}) were obtained from Addison Engineering, Inc. Immediately before transfer of Gr or h-BN, the native oxide on the p-Si wafer pieces was etched using improved buffered HF (BHF, Transene). BHF was also used to clean bare p-Si electrodes immediately before electrochemical testing.

CVD-grown monolayer Gr on Cu (Cu/Gr) and CVD-grown monolayer h-BN on Cu (Cu/h-BN) were purchased from Advanced Chemical Supplier Materials (Medford, MA). Grains of Gr from

this source are ~ 50 μm in diameter, as reported by the manufacturer, while grains of h-BN from this source are ~ 4 μm in diameter.

Electrode fabrication

Ohmic back contacts to the p-type Si wafers were formed by evaporation of 100 nm of Au (Labline Electron Beam Evaporator, Kurt J. Lesker) followed by an anneal at 350 °C under forming gas (H_2(g):N_2(g) v:v 5:95). Wafer pieces used for SECCM measurements were additionally lithographically patterned with registry marks, to track the location of the electrochemical measurements and ensure that data were collected on intact portions of the 2D material monolayer.

The h-BN used in this study was grown on Cu, analogously to the Gr, hence electrodes for both 2D materials were made by a similar process. The methods for the Gr electrodes are described in detail below. To make the coated electrodes, a strip of Cu covered by monolayer Gr (Cu/Gr) was coated with a supporting polymer layer of 495K A4 polymethyl methacrylate (PMMA, MicroChem) at 3000 rpm for 60 s. The resulting stack (Cu/Gr/PMMA) was then cured for 5 min at 120 °C. Smaller pieces, which matched the desired size of the electrodes being fabricated, were cut and etched in a $FeCl_3$ etch solution (Copper etch, Transene) until the Cu disappeared by visual inspection, generally requiring ~ 1.5 h. This Cu-free piece (Gr/PMMA) was transferred to a ≥18.2 MΩ-cm resistivity H_2O bath for 1 h before transfer to a second clean H_2O bath into which the sample was immersed for 12 h. After transfer to a final fresh H_2O bath, the stack was pulled onto a p-Si wafer piece that had been etched with improved buffered HF, dried thoroughly using a gentle stream of N_2(g), and heated to 80 °C for 10 min to allow the PMMA layer to reflow. The substrate was then rinsed in acetone for 10 min before being annealed for 2 h at 350 °C in a

reducing atmosphere (H_2(g):Ar(g) v:v 5:95), to remove any residual PMMA from the transfer process.

The p-Si/Gr stack was attached to a Cu wire using a Ga-In eutectic alloy and high-purity Ag paint (SPI Supplies, West Chester, Pennsylvania). The back of the electrode was covered with a layer of clear nail polish to minimize leakage of the Ga-In eutectic. The sample was then sealed to a Pyrex tube with a layer of Loctite 9460 Hysol epoxy and cured overnight. The area of the resulting electrode was measured using ImageJ software for analysis of optical images of each electrode.

For the macroscale measurements, a set of control electrodes (p-SiO_x), which were exposed to the same transfer process without the introduction of a 2D material, were made by otherwise nominally identical processes to those used to make the p-Si/Gr and p-Si/h-BN electrodes described above. In brief, a layer of PMMA was spun onto a bare Cu foil to generate a Cu/PMMA stack. This stack was processed identically to the Cu/Gr/PMMA stacks, yielding p-Si–H samples that did not contain a 2D overlayer. These samples will be referred to as p-SiO_x, or blank electrodes, as the processing and annealing steps generated a small amount of silicon oxide on the surface, in contrast to the p-Si–H electrodes, which immediately prior to testing were etched with improved buffered HF to remove any residual oxide.

SECCM samples were made analogously to the bulk process above, with the Gr and h-BN samples transferred to the same p-Si wafer chip to ensure uniformity between the two materials. After annealing, the sample was attached through the back contact to a custom SECCM stage for analysis.

For Hall measurements, samples were prepared using the methods described above to transfer Gr to p-Si that was coated with a 300 nm thermal oxide. Au top contacts and a thin Ti adhesion layer were deposited by e-beam evaporation.

For UV/Vis measurements, samples were prepared using the methods described above to transfer Gr or h-BN to a quartz slide before processing and annealing as before.

For surface recombination velocity (SRV) measurements, samples were prepared as above and transferred to floatzone-grown, double-side polished Si wafers that were not intentionally doped, had a resistivity of 20 kΩ cm, and were 300 ± 25 μm thick (Semiconductor Processing Co.) before processing and annealing as before.

Electrochemical Methods

Bulk electrolysis was performed in a four-necked round-bottom flask inside a N_2(g)-purged flush box that contained <3 ppm O_2(g). The working and counter electrodes were Pt meshes, and the reference electrode was a Pt-polypyrrole (Pt-PPy) electrode prepared in a CH_3CN–0.50 M $LiClO_4$ solution.[24] The reference and counter electrodes were each contained in separate compartments constructed from borosilicate tubing, with a Vycor porous glass frit attached to the end of the glass tubing by use of Teflon heat-shrink tubing. Each compartment was filled with CH_3CN–0.50 M $LiClO_4$. The bulk electrolysis was monitored by cyclic voltammetry using a 12.5 μm radius Au ultramicroelectrode.

All macroscale measurements were performed inside an Ar-filled dry box with <0.5 ppm O_2(g), with leads connected externally to a SP-200 Biologic potentiostat. The reference electrode was Pt-PPy, deposited from a 10 mM solution of pyrrole in CH_3CN–0.50 M $LiClO_4$.[24] The reference

electrode was remade for use with each redox couple, and consistently produced a stable potential of ~+0.20 V vs. Ag/AgCl. For each redox couple, cyclic voltammograms on p-Si–H, p-SiO_x, p-Si/Gr, and p-Si/h-BN were recorded at a 50 mV s^{-1} scan rate either under illumination or in the dark. The V_{oc} was measured multiple times for each electrode, although the duration of the measurements was adjusted for different redox couples to allow ample time for V_{oc} to stabilize.

Pipettes for SECCM were prepared using a Sutter Instruments P-2000 laser puller. Quartz theta capillaries (1.2 mm outer diameter, 0.9 mm inner diameter; Sutter Instruments) were first cleaned with acetone and methanol, and were then pulled to create pipettes having openings between 50-500 nm in radius. The pipettes were then silanized with chlorotrimethylsilane to create a hydrophobic surface.[25] Pipettes were filled with electrolyte solutions using a glass syringe and a stainless-steel needle.

All SECCM measurements were performed using a CHI 920D potentiostat inside a N_2(g)-purged flush box that contained < 3 ppm O_2(g). The counter and reference electrodes were 0.2 mm diameter Pt wires, each on opposite sides of the theta pipette, and the p-Si photoelectrode was the working electrode. Prior to approaching the surface, an endoscope was used to position the pipettes to within 20 μm of the desired location. As pipettes were approached to the surface, the substrate was then biased positive with respect to the reference electrode. Movement automatically stopped when the potentiostat detected the current spike that occurred when a liquid junction formed. The size of the liquid junction was approximated from the anodic i_{ss} of the redox couple as measured from a linear sweep voltammogram taken in the dark using the equation $i_{ss}=4nFaDc^*$, where n is the number of electrons transferred per oxidation, F is Faraday's constant, a is the radius of the tip, D is the diffusion coefficient of the redox species, and c^* is the bulk concentration of the redox species. Only measurements taken using junctions with radii of a <200 nm were included in

this study, as larger junctions were unstable. Illumination for photoelectrochemical SECCM experiments was provided at a 45° angle by a fiber optic attached to an ELH-type W-halogen lamp with a dichroic rear reflector, with the entire optical train and light source located inside the flush box. The measured illumination intensity was equivalent to 100 mW cm^{-2} of Air Mass 1.5 sunlight as measured by a NIST-calibrated photodiode. As in the macroscale measurements, cyclic voltammograms at each location using each redox couple were recorded at a 50 mV s^{-1} scan rate either in the presence or absence of illumination. Open-circuit voltage measurement times were adjusted for different redox couples and locations to allow sufficient time for V_{oc} to stabilize in each case.

Instruments

XPS data were collected at $1x10^{-9}$ Torr using a Kratos AXIS Ultra DLD with a magnetic immersion lens that consisted of a spherical mirror and concentric hemispherical analyzers with a delay-line detector (DLD). An Al Kα (1.486 KeV) monochromatic source was used for X-ray excitation. Ejected electrons were collected at a 90° angle from the horizontal. The CASA XPS software package v 2.3.16 was used to analyze the collected data.

Carrier mobilities were obtained using an H-50 MMR Hall Measurement System. Raman spectra were collected with a Renishaw Raman microscope at a wavelength of 532 nm through an objective with numerical aperture of 0.75. The laser power was ~3 mW. UV/Vis transmission spectra were collected with a Cary 5000 absorption spectrometer equipped with an external DRA 1800 attachment. The data were automatically zero/baseline corrected by the instrument before any additional processing was performed. Surface recombination velocity (S) measurements were collected with a contactless microwave conductivity apparatus, which used a 20 ns laser pulse at

905 nm generated by an OSRAM laser diode and an ETX-10A-93 driver to form electron−hole pairs. The charge-carrier lifetime was determined by monitoring the change in reflected microwave intensity using a PIN diode connected to an oscilloscope. The data was collected using a custom LabView program. All photoconductivity decay curves were averages of 16 consecutive decays.

Results

Characterization

X-ray photoelectron spectroscopy, Raman spectroscopy, and UV/vis spectroscopy collectively indicated that the polycrystalline monolayers used in this work were intact over areas exceeding the area expected for a single grain (~25-2500 μm^2) and displayed the expected electrical characteristics for Gr and h-BN (Figure S1-S6), respectively. The h-BN monolayers had a band gap of 6.07 eV and transmitted ~100% of the light between 250-1200 nm in wavelength as determined by UV/Vis spectroscopy. Gr had no band gap and transmitted ~97% of light over the same region. Measurements of the Hall mobility of Gr were collected for four different samples with electrodes in a van der Pauw configuration, and yielded an average value of 9.7×10^2 cm^2 V^{-1} s^{-1}, which falls within the range expected for monolayer polycrystalline Gr transferred using a wet chemical method (500-10,000 $cm^2/V \cdot s$).[26-28] Ultraviolet photoelectron spectroscopy (UPS) was used to measure the band positions and to determine any effects of the fabrication process of each type of sample (Table S1). The p-Si–H samples exhibited a work function of 4.40±0.07 eV whereas p-SiO_x, p-Si/Gr, and p-Si/h-BN had work functions on average of 4.92±0.0017 eV, 4.73±0.007 eV, and 4.77±0.006 eV, respectively.

Electrochemistry

Figure 1 presents the representative macroscale current density versus potential (*J*-*E*) behavior for p-Si–H, p-SiO_x, p-Si/Gr, and p-Si/h-BN electrodes, respectively, in the dark and under 100 mW cm^{-2} of ELH-type W-halogen simulated solar illumination in CH_3CN–0.50 M lithium perchlorate solutions containing either ferrocene$^{+/0}$ or cobaltocene$^{+/0}$. The samples referred to as p-SiO_x, or "blank" electrodes, in reference to the small amount of oxide grown on the surface during fabrication (*vide supra*), are also included in the macroscale measurements to show the behavior of a p-Si–H electrode when subjected to nominally the same processing steps as the p-Si/Gr and p-Si/h-BN electrodes in the absence of transferring a 2D overlayer to the surface (Figure S7). For macroscale electrodes, the bare p-Si–H and p-SiO_x electrodes exhibited rectifying behavior toward both redox couples, as indicated by increased cathodic photocurrent under increasing negative potentials (i.e. increasing reverse bias). As expected from the relative position of the Fermi level of p-Si with respect to the redox couples shown, the shift in the open-circuit voltage, V_{oc}, measured relative to the Nernstian potential of the solution, $E(A/A^-)$, for these electrodes under illumination was larger in contact with $Cp_2Co^{+/0}$, which has a more negative effective redox potential, E_{eff}, (see SI and Ref. 31 for calculation of the concentration-corrected effective redox potential, E_{eff}, relative to the Nernstian potential of the solution, $E(A/A^-)$), than for $Cp_2Fe^{+/0}$. In contact with $Cp_2Fe^{+/0}$, p-Si/h-BN electrodes exhibited minimal rectification and displayed substantial currents under reverse bias in the dark. In contact with $Cp_2Co^{+/0}$, these electrodes showed strong rectification, with only minimal dark current and a large photocurrent. In contrast, the p-Si/Gr samples exhibited ohmic behavior in the $Cp_2Fe^{+/0}$ solution and moderately rectifying behavior in contact with the $Cp_2Co^{+/0}$ solution, as shown by the rapid increase in currents under forward bias for both of these sample types in the dark.

Similar was observed behavior for all samples by SECCM, except for the p-Si/Gr interface (Figure 2). The macroscale measurements are shown as current density versus potential, whereas due to effect of pipette tip size on resulting current density, the SECCM data are displayed using current normalized to the transport-limited steady-state current (i/i_{ss}) observed during cathodic operation under illumination.[29-30]

During macroscale testing, six replicate photoelectrodes were tested for each redox couple. Individual photoelectrodes were used to measure V_{oc} against at most two redox couples, and were rinsed between testing with copious amounts of CH_3CN. Each photoelectrode was not used with more than two couples to avoid testing samples that may have degraded through use. This procedure guards against using samples in which Gr delaminated from the Si surface due to the capillary forces produced as the electrolyte solvent dries after cleaning or moving a single sample between different solutions. Because of this precaution, the values for V_{oc} have not been collected against the full range of redox couples for any single electrode. In contrast, due to the small spot size of SECCM, the full complement of redox couples were measured on a single 1 cm^2 sample that contained bare regions as well as regions covered separately by Gr and h-BN, thereby allowing their distinct behaviors to be elucidated.

Figure 3 shows the dependence of V_{oc} on the effective solution potential for macroscale p-Si–H, p-SiO_x, p-Si/Gr, and p-Si/h-BN electrodes, respectively, in contact with CH_3CN–0.50 M $LiClO_4$ under 100 mW cm^{-2} of ELH-type W-halogen simulated solar illumination. Each point represents an average of at least 5 electrodes, with standard deviations represented by the error bars. The V_{oc} data for all redox couples are summarized in Table 1. In the macroscale measurements, the p-Si–H, p-SiO_x, and p-Si/h-BN samples showed two distinct trends: regions at relatively positive or negative $E_{eff}(A/A^-)$ in which V_{oc} was fixed with respect to $E_{eff}(A/A^-)$; and a second region in which

V_{oc} scaled approximately linearly with $E_{eff}(A/A^-)$. The slopes of V_{oc} with respect to $E_{eff}(A/A^-)$ for p-Si–H surfaces were lower than those reported previously, but the maximum ΔV_{oc} of 505±53 mV is comparable with the previously reported value of 523±42 mV.[31] The p-Si–H, p-SiO_x, and p-Si/h-BN samples evaluated in this work displayed slopes, $-\Delta V_{oc}/\Delta E_{eff}(A/A^-)$, of ~0.41, 0.43, and 0.45, respectively, while the p-Si/Gr samples had a lower slope of $-\Delta V_{oc}/\Delta E_{eff}(A/A^-) \sim 0.24$ (Table S2). These electrodes also displayed the smallest change in V_{oc} across the full range of redox couples, with V_{oc} shifting only in contact with redox couples that had the most negative $E_{eff}(A/A^-)$ values ($E_{eff} \leq$ -0.35 vs. SCE).

Figure 4 shows the dependence of V_{oc} on $E_{eff}(A/A^-)$ for nanoscale p-SiO_x, p-Si/Gr, and p-Si/h-BN electrodes, respectively, in contact with CH_3CN–0.50 M $LiClO_4$ under 100 mW cm^{-2} ELH-type illumination. The data for the nanoscale measurements displayed the same three regions observed in the macroscale V_{oc} measurements (Figure 3). The maximum ΔV_{oc} for p-Si–H by SECCM was 342±18 mV, which is closer to 401±33 mV, the maximum ΔV_{oc} value for the macroscale p-SiO_x measurements than it is to the macroscale p-Si–H measurements. This behavior can be understood from the preparation of the SECCM sample. As the p-Si–H, p-Si/Gr, and p-Si/h-BN measurements were all taken on the same wafer chip, to ensure uniformity in sample preparation, the p-Si–H surface could not immediately be etched before testing by SECCM, leaving a small amount of oxide on the surface, similar to the preparation of the p-SiO_x electrodes used in the macroscale electrode measurements. Table 1 summarizes the experimental conditions and all V_{oc} data for the macroscale and SECCM measurements.

Discussion

The data shown above clearly demonstrate that in otherwise nominally identical interfaces, Gr shows markedly different behavior from h-BN. The higher density of states in Gr introduces surface states that decrease V_{oc} in both macroscale and nanoscale measurements. These data also indicate that the nanoscale and macroscale data show excellent congruency. Despite the extremely small contact area, nanoscale measurements consistently showed the same junction behavior as their macroscale counterparts. Solid-state point contacts can show ohmic behavior at otherwise rectifying junctions, so the ability to reliably produce nanoscale junctions that show the same behavior as their macroscale counterparts is significant. Although multiple effects may contribute to the quantitative differences between the measured quantities, the measurements are robust enough to reveal important differences between different interfaces and different scales.

Macroscale measurements

The macroscale behavior of p-Si photoelectrodes can be divided into two groups: photoelectrodes with parallel slopes of $\Delta V_{oc}/\Delta E_{eff}(A/A^-)$ (p-Si–H, p-SiO_x, and p-Si/h-BN) and those without (p-Si/Gr). The differences in the values for V_{oc} between the macroscale p-Si/Gr and p-Si/h-BN samples can arise from the presence of oxide at the p-Si surface, increased surface recombination due to the surface oxide or defects in the polycrystalline 2D overlayer, and differences in the relative density of states of each polycrystalline 2D overlayer. Due to the nominally identical p-Si source and fabrication process, the effect of the oxide on V_{oc} can be quantified by directly comparing the p-Si–H and p-SiO_x electrodes to show that V_{oc} was attenuated by ~ 0.1 V in the presence of a thin oxide. XPS analysis showed that the p-SiO_x, p-Si/Gr, and p-Si/h-BN electrodes all had similar amounts of oxide at the surface (Figure S1), hence this same decrease in V_{oc} is expected for the measurements at both the p-Si/Gr and p-Si/h-BN interfaces. However, this decrease in V_{oc} due to surface oxide does not fully account for the differences observed between

the p-Si–H and p-Si/2D overlayer (p-Si/2D) photoelectrodes. The p-Si/h-BN interfaces showed an additional 65 mV decrease in V_{oc} compared to p-SiO_x. The similarity in $\Delta V_{oc}/\Delta E_{eff}(A/A^-)$ for the p-Si–H, p-SiO_x, and p-Si/h-BN electrodes suggests that the change between p-SiO_x and p-Si/h-BN should be treated as a linear decrease in the overall performance as compared to p-Si–H electrodes, analogous to the behavior when oxide is introduced onto a H-terminated p-Si electrode.[32] This h-BN overlayer is the primary difference between the p-SiO_x and p-Si/hBN electrodes, which after annealing have mutually similar work functions and dipoles (Table S1). Thus, the additional 65 mV loss in V_{oc} is attributable to the effects of the h-BN. Pristine h-BN does not have surface states within the band gap of Si, hence the small change in V_{oc} is likely the result of small increases in trap-state-mediated recombination (J_{br}), and thus J_0, due to the polycrystalline nature of the h-BN used in this work. Polycrystalline, CVD-grown sheets of monolayer 2D material contribute to defects on the surface of a 2D material and provide sites for increased surface recombination.[16, 33] This behavior is consistent with expectations in which changes in the surface recombination velocity, S, affect V_{oc} but do not substantially affect the work function of a sample.[34-35] p-SiO_x samples have a slightly lower S (= 3025 cm s^{-1}) than the p-Si/h-BN samples (S = 3905 cm s^{-1}). Similarly, J_0 is higher by an order of magnitude for p-Si/h-BN in contact with $Cp_2Co^{+/0}$ than J_0 for either p-Si–H or p-SiO_x.

Although the surface recombination velocity of p-Si/Gr (4064 cm s^{-1}) is similar to that of p-Si/h-BN, and this interface has the same work function as p-SiO_x and p-Si/h-BN, the p-Si/Gr electrodes display a lower value of $\Delta V_{oc}/\Delta E_{eff}(A/A^-)$ over the same range of effective potentials, suggesting the predominance of a different mechanism to determine V_{oc} for these macroscale junctions. The fit chosen for the macroscale p-Si/Gr data is discussed in detail in the SI. The polycrystallinity of the Gr and h-BN used in this work could contribute to the smaller value for V_{oc} or range of tunable

V_{oc} when compared to p-Si–H or p-SiO_x electrodes, but cannot readily account for the differences between the p-Si/Gr and p-Si/h-BN samples, because the grains of the h-BN used in this work were an order of magnitude smaller than those in the Gr. If the crystallinity were the sole factor in limiting the range of potentials at the interface, p-Si/h-BN would have lower values of V_{oc}, and higher surface recombination velocities than p-Si/Gr samples, in contrast to the experimental observations.

Measurements of the barrier height of n-Si/2D/metal Schottky diodes exhibit trends that are in accord with the observations reported herein for semiconductor/liquid interfaces.[6] The decrease in barrier height of both n-Si/2D/metal and p-Si/2D/liquid junctions suggests that limitations imposed by device fabrication, rather than intrinsic polarization of the 2D overlayer, dominates the formation of the interface dipole. Thus, the decrease in V_{oc} due to a surface dipole is more consistently ascribed to increased surface recombination at the interface as opposed to the intrinsic nature of the 2D material. The surface oxide, increase in recombination, and polycrystalline nature of the 2D overlayer only partially account for the difference between p-Si–H and p-Si/Gr or p-Si/h-BN, so the properties of the 2D material and interaction with the surface contribute substantially to the observed differences in behavior of the semiconductor/liquid interfaces investigated herein. The crystal structure and lattice constants for Gr and h-BN are nearly identical and these 2D materials differ most prominently in their respective band gap (Figure S6). With a limited density of states near its Fermi level, which is positioned mid-gap to silicon, the Gr in these junctions exerts more influence on the interfacial energetics than h-BN, which has no states mid-gap or near the conduction or valence band of Si. This characteristic leads to a more negative onset in the slope of V_{oc} as well as a shallower slope of $\Delta V_{oc}/\Delta E_{eff}(A/A^-)$.

Nanoscale measurements

As shown in Figure 3 and 4, the fixed and sloping regions of V_{oc} with respect to solution potential measured by SECCM generally were in excellent agreement with their macroscale counterparts. However, the values for V_{oc} of p-Si–H at the macroscale were consistently higher than those observed by SECCM. The values of V_{oc} for p-Si–H by SECCM were much closer to the values of V_{oc} for the macroscale p-SiO_x electrodes. This similarity follows from the XP spectra (Figure S1), which shows that the same or a greater thickness of oxide was generated at the surface of the p-SiO_x electrodes as the p-Si/Gr and p-Si/h-BN electrodes during fabrication. Thus, the bare region of the single electrode used for SECCM was more similar to the Si surface under Gr or h-BN than to a freshly etched p-Si–H electrode. The presence of a surface oxide can thus consistently account for a decrease in observed V_{oc} of ~ 100 mV for both p-Si/Gr and p-Si/h-BN electrodes.

Certain specific measurements, such as the V_{oc} of p-Si/h-BN in contact with $Cp_2Ni^{+/0}$, were lower for macroscale electrodes than were observed by SECCM. These differences were predominantly observed for the less stable redox couples (i.e. $Cp^*_2Co^{+/0}$, $Cp_2Ni^{+/0}$). The slopes in V_{oc} for p-Si–H, p-SiO_x and p-Si/h-BN were identical, within experimental error, for the macroscale and SECCM measurements, demonstrating that the observed trends were mutually consistent the same across the macro and nanoscale.

The voltammetry (Figure 1-2) showed identical shapes between macroscale and SECCM measurements but revealed different behavior between the different types of electrode. The p-Si–H was strongly rectifying in contact with $Cp_2Co^{+/0}$ and had a high value of V_{oc} under illumination. The p-Si/h-BN was also rectifying, but the shape of the *J-E* characteristic under illumination indicated much more resistive behavior than was observed for p-Si–H electrodes. Specifically, a light-limited current was not reached until the potential was further negative than the window shown. The p-Si/Gr interface was rectifying to $Cp_2Co^{+/0}$ and had a large dark saturation current

density ($J_0 \sim$ -5 mA cm^{-2}) relative to the other interfaces ($J_0 \sim$ -5x10^{-3} mA cm^{-2} for p-Si–H and p-SiO_x; $J_0 \sim$ -5x10^{-2} mA cm^{-2} for p-Si/h-BN). In contact with $Cp_2Fe^{+/0}$, all samples were ohmic and displayed similar fill factors to the voltammetry in contact with $Cp_2Co^{+/0}$. A spatial comparison of this behavior (Figure S9) demonstrated that the V_{oc} did not vary substantially across the surface in either sample, despite the presence of grain boundaries in the polycrystalline material. This uniformity, alongside the agreement between nanoscale and macroscale V_{oc} trends, provides support for the observation that grain boundaries in the 2D materials are not strongly contributing to the PEC behavior, as the SECCM measurements are made on a scale well below the size of individual grains of either Gr or h-BN. The ability of these liquid probes to replicate the ohmic or rectifying behavior of macroscale junctions is notable. Previous reports employing conductive AFM with Ni tips on n-Si/Gr showed ohmic behavior whereas macroscale n-Si/Gr/Ni junctions showed rectifying behavior.[12] Hence in contrast to metal probes, liquid probes provide more reliable information about nanoscale junction behavior and enhance the understanding of how nanoscale spatial heterogeneity of interstitial layers impacts macroscale junction behavior.

Although the magnitude of V_{oc} measured using SECCM is not in precise agreement with that of macroscale measurements, several differences between these techniques could be responsible for the observed differences. Two cases in which the difference deviated from the observed trend are consistent with effects associated with the use of specific redox couples in the nanoscale junction (see SI). However, systemic differences were also observed. The most apparent difference in experimental conditions between the macroscale and SECCM measurements is the geometry of carrier transport due to the size of the liquid junction. In the macroscale case, the photoelectrochemical junctions are much larger than the depletion width (W) of Si so carrier transport and band bending are one-dimensional. Because the radius of the liquid junction in our

SECCM measurements is typically smaller than W (between 100 and 185 nm for the couples used), band bending will occur in a hemispherical volume of radius W centered around the liquid nanojunction, as is seen using metal probes in SPM.[36-37] This geometry increases the number of carriers that can be collected at the interface relative to the 1D case. In contrast, SECCM measurements showed the same ohmic or rectifying behavior as the macroscale counterpart.

Despite this qualitative agreement in junction behavior, this transport geometry causes a secondary effect that impacts the magnitude of V_{oc} measured at the nanoscale. For all rectifying junctions, the V_{oc} measured by SECCM is lower than that observed by macroscale. This difference is consistent with expectations for effects produced by hemispherical band bending occurring entirely within a distance of W from the Si surface. Hemispherical band bending provides substantially more opportunity for recombination than a 1D case, due to the increase in surface area relative to volume. This increase in recombination decreases the collection efficiency of photogenerated electrons relative to the more plentiful holes and ultimately would decrease the V_{oc}.[38] As they are similarly affected, the drop in V_{oc} is nearly identical for p-SiO_x and p-Si/h-BN. While p-Si/Gr electrodes are affected by this process, they also show nonzero values for V_{oc} of 0.021±0.004 V by SECCM in the lower plateau in which junctions exhibit ohmic behavior, as opposed to the 0.006±0.007 V observed in macroscale measurements. This nonzero plateau could arise from the combination of overfill illumination and the high conductivity of Gr enabling lateral conduction of carriers from a significantly larger region of the sample than expected from the size of the liquid junction. Transfer of photogenerated electrons from the Si to the Gr would compete with recombination and enhance the photocurrent at the liquid junction, thus increasing the measured V_{oc}. Both of the above cases represent fundamental limitations of nanoscale junctions on macroscale photoelectrodes. Future studies utilizing finite element modeling could potentially

deconvolute these effects from other differences at the surface, as has been been done previously to improve understanding of carrier transport in other scanning probe microscopies.[39-40] Despite the present limits of this technique, the agreement between trends in V_{oc} vs. E_{eff} for macroscale and SECCM measurements shows that despite the difference in carrier transport the same trend is observed between nanoscale and macroscale contacts.

Conclusions

Compared to H-terminated p-Si electrodes using the same electrolyte, the V_{oc} values of p-Si electrodes coated with highly conductive or insulating 2D materials, graphene (E_g 0 eV) and hexagonal boron nitride (E_g 5.97 eV) respectively, demonstrate that the properties of these interfaces are dependent primarily on the position of the Fermi level and density of states of the 2D material relative to band edges of the chosen semiconductor. Both Gr and h-BN-coated p-Si photoelectrodes displayed lower open circuit-voltages in contact with a series of redox couples in solution than bare p-Si–H photoelectrodes. Gr coated p-Si electrodes have a high density of states at the 2D material, causing some Fermi level pinning. Despite the high density of states of graphene, the pinning is moderate because only a single layer of atoms is required for full surface coverage, ultimately minimizing the density of states introduced at the surface. Hence even highly conductive 2D materials can be useful as protecting layers with minimal effects due to Fermi level pinning. For h-BN coated p-Si electrodes, the 2D material has a low density of states, and thereby avoids pinning due to introduced surface states. However, the oxide formed during transfer of either 2D material and subsequent processing of the electrode interacts with the electrical character of the 2D material to introduce surface dipoles that shifts the band positions of the semiconductor surface to more negative values. These results indicate that exploration of 2D materials with greater differences in electronegativity, in conjunction with transfer methods that prevent oxide

formation, could allow facile tuning of band energetics through the use of 2D materials as protecting layers for semiconductors.

SECCM can thus provide a useful technique for evaluation of the V_{oc} of 2D semiconductor photoelectrodes. These results provide a definitive demonstration of V_{oc} measurements by SECCM, in conjunction with a unique ability among microscopy techniques to assess the utility of nanoscale heterojunctions to replicate the ohmic or rectifying behavior of macroscale measurements using nominally identical electrodes and electrolyte solutions in each case. This feature makes, for the first time, reliable measurements of nanoscale photoelectrochemistry viable, and provides a path to studying materials with nanoscale heterogeneity that impacts macroscale performance. Additionally, nanoscale SECCM measurements of V_{oc} replicate trends observed at the macroscale, though quantitative differences are evident in the case of Gr. Moreover, SECCM allowed measurement of the variation in V_{oc} between coated and uncoated regions of a 2D material on a single p-Si electrode, demonstrating applicability for imaging semiconductor/liquid junction energetics with nanoscale resolution.

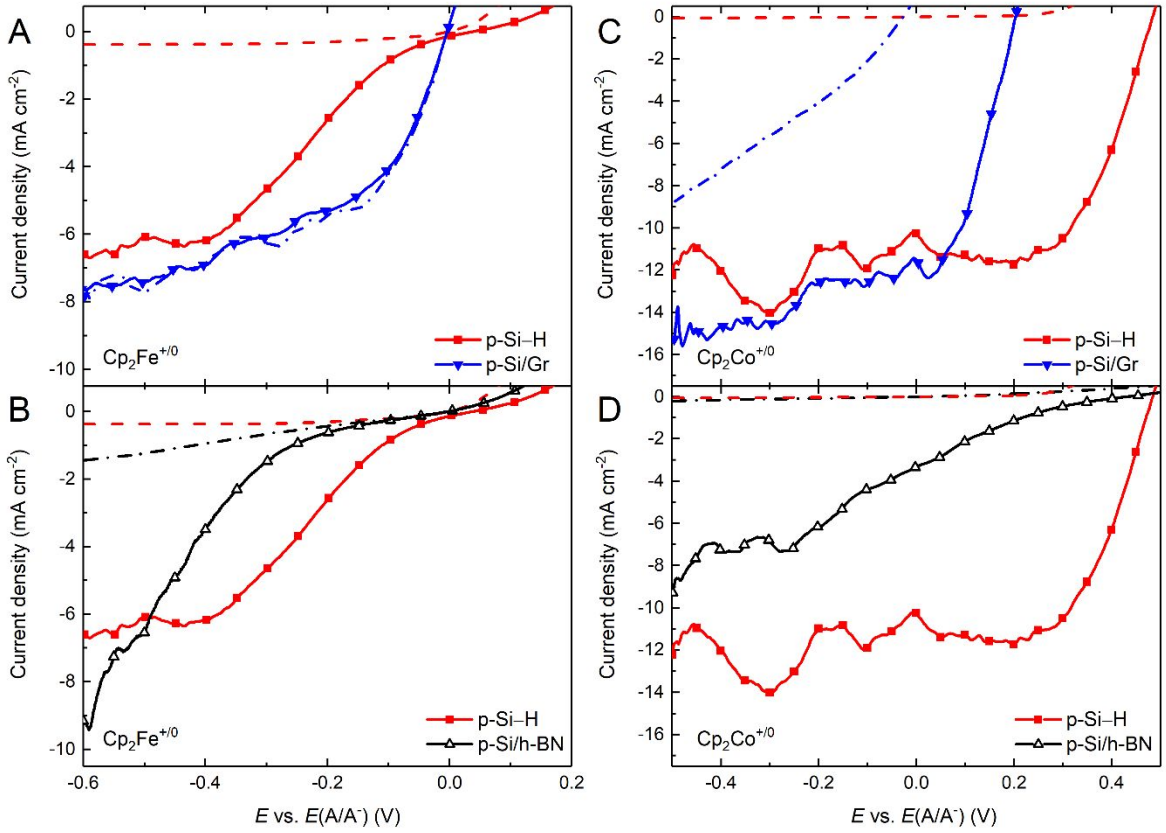

Figure 1. Current density vs potential (*J-E*) behavior of modified p-Si electrodes in contact with $Cp_2Fe^{+/0}$ (A-B) and $Cp_2Co^{+/0}$ (C-D), in CH_3CN–0.50 M $LiClO_4$ under 100 mW cm^{-2} of ELH-type simulated solar illumination. The dashed lines show scans of the same electrodes without illumination. In contact with either redox couple, the fill factor of the p-Si/h-BN electrode was substantially smaller than that of either the p-Si–H (Figure 1) or p-SiO_x (Figure S7) electrodes, indicative of slow electron-transfer kinetics at the h-BN/liquid interface. In contact with $Cp_2Co^{+/0}$, the *J-E* characteristics of the p-Si/Gr electrode shifted upon illumination, in addition to displaying substantially larger reverse saturation current densities than the other three types of electrodes.

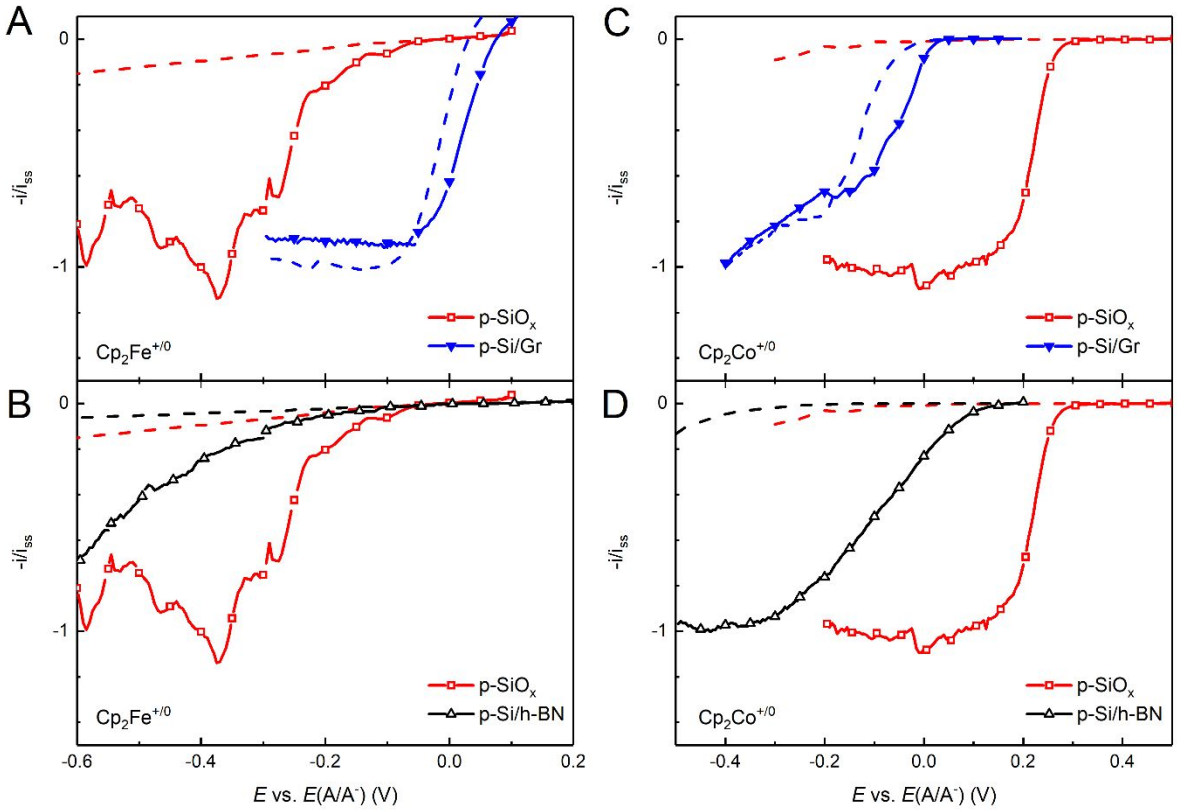

Figure 2. Current vs potential (*I-E*) behavior in contact with CH_3CN–0.50 M $LiClO_4$ under 100 mW cm^{-2} of ELH-type simulated solar illumination determined by SECCM for p-Si electrodes in contact with $Cp_2Fe^{+/0}$ (A-B) and $Cp_2Co^{+/0}$ (C-D). The dashed lines show scans of the same electrodes without illumination. The data in SECCM measurements were similar to data observed in the macroscale measurements (Figure 1). Si–H surfaces were not probed by SECCM because the O_2 and water content in the flush box used for these experiments resulted in the formation of oxide on freshly etched Si–H samples more rapidly than measurements could be performed.

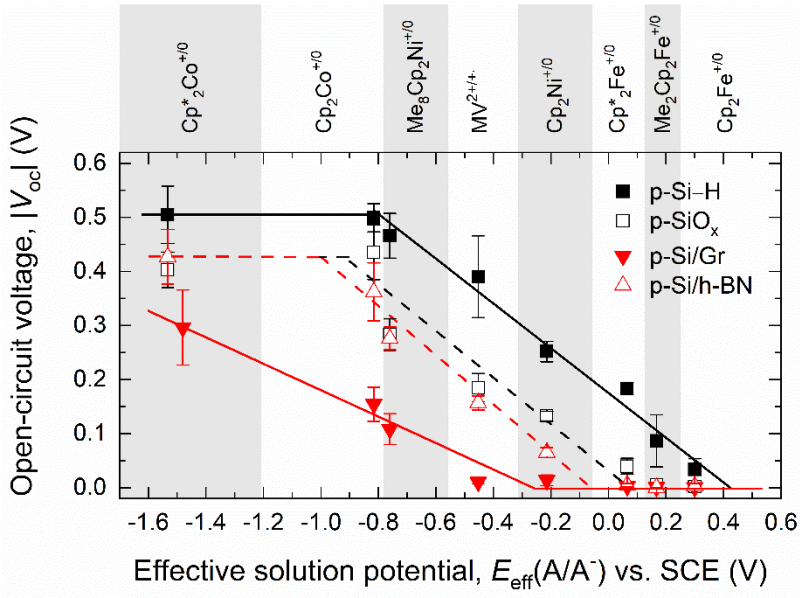

Figure 3. Comparison of open-circuit voltage of macroscale p-Si–H, p-SiO_x, p-Si/Gr, and p-Si/h-BN electrodes, respectively, versus the effective redox potential of various redox couples. Three regions, each highlighted by linear fits of the data therein, were identified for all samples.

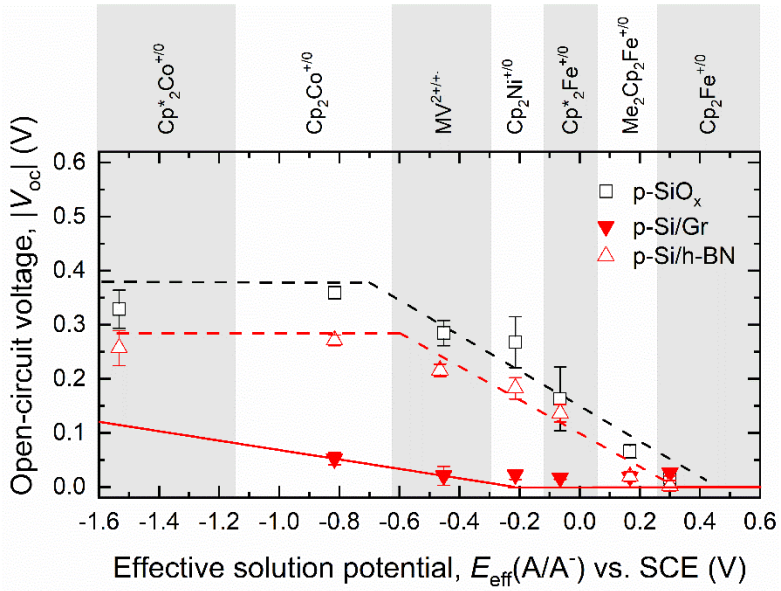

Figure 4. Comparison of the open-circuit voltage of p-SiO_x, p-Si/Gr, and p-Si/h-BN electrodes, respectively, versus the effective potential of various redox couples, on the same SECCM electrode. Linear fits of the data have been used to highlight the different regions of behavior.

Table 1. Summary of experimentally measured V_{oc}[a]

Redox couple[a]	effective potential vs. SCE[b] (V)	V_{oc} (V) from macroscale electrodes				V_{oc} (V) from SECCM electrode		
		p-Si–H	p-SiO_x	p-Si/Gr	p-Si/h-BN	p-Si–H	p-Si/Gr	p-Si/h-BN
$Cp^*_2Co^{+/0}$	-0.963	0.505(53)	0.403(33)	0.296(70)[c]	0.427(50)	0.329(35)	-[d]	0.257(32)
$Cp_2Co^{+/0}$	-0.816	0.499(26)	0.436(50)	0.154(32)[c]	0.362(54)[c]	0.360(11)	0.052(11)	0.272(10)
$Me_8Cp_2Ni^{+/0}$	-0.760	0.466(41)	0.283(29)	0.108(28)	0.276(21)	-	-	-
$MV^{2+/+\bullet}$	-0.453	0.390(76)	0.185(26)	0.011(3)	0.157(13)	0.285(23)	0.021(18)	0.216(11)
$Cp_2Ni^{+/0}$	-0.214	0.252(19)	0.133(9)	0.014(10)[c]	0.065(9)[c]	0.268(47)	0.023(9)	0.183(20)
$Cp^*_2Fe^{+/0}$	0.065	0.183(11)	0.040(14)	0.003(1)	0.005(3)	0.163(60)	0.017(3)	0.136(16)
$Me_2Cp_2Fe^{+/0}$	0.167	0.087(48)	0.005(3)	0	0	0.066(12)	0.018(5)	0.019(9)
$Cp_2Fe^{+/0}$	0.171	0.034(20)	0.002(1)	0	0.003(5)	0.018(14)	0.026(5)	0.002(10)

[a] Each value of V_{oc} represents measurements from at least six photoelectrodes on the macroscale and at least three spots by SECCM. Standard deviations are given in parentheses, where appropriate, and are in units of mV. Abbreviations for the couples used are given in the Methods section.

[b] The effective cell potential was calculated using the equation $E_{eff}(\mathrm{A/A^-}) = E(\mathrm{A/A^-}) - \frac{k_B T}{q} \ln \frac{[A_{eff}]}{[A]}$, where E(A/A$^-$) was the cell potential of the redox couple vs. SCE, [A] was the minority acceptor concentration, and [A_{eff}] = 10 mM. These values are reported vs SCE, which taken to be +0.197 V vs. NHE in this work.

[c] In select instances for macroscale testing, new solutions with slightly different potentials than those listed here were made to retest certain electrodes. The potentials of these solutions are not tabulated here but are shown correctly in Figure 3.

[d] Due to the lack of stability in the $Cp^*_2Co^{+/0}$ couple, no SECCM measurements could be collected for the p-Si/Gr interface

ASSOCIATED CONTENT

Supporting Information.

The Supporting Information is available free of charge on the ACS Publications website at DOI: 10.1021/acsnano.XXXXXXX.

- Figures S1-S6 and Table S1 contain XPS, UPS, Raman maps, UV-Vis spectra, and Tauc plots characterizing the 2D materials and 2d material coated p-Si
- Figure S7 contains data for cyclic voltammetry of p-SiO_x electrodes
- Figure S8 and Table S2 contain alternate linear fits and their parameters for V_{oc} measurements on macroscale p-Si/Gr electrodes
- Figure S9 contains V_{oc} data taken in line scans using SECCM
- S1 discusses the calculation of effective solution potentials and Table S3 contains experimental redox couple concentrations, the standard reduction potential, and the effective solution potential calculated from these numbers
- S2 discusses redox couple compatibility with nanoscale junctions

nnXXXXXXX.pdf (PDF)

AUTHOR INFORMATION

Corresponding Author

*E-mail: nslewis@caltech.edu

Author Contributions

The manuscript was written through contributions of all authors. All authors have given approval to the final version of the manuscript. ‡These authors contributed equally. (match statement to author names with a symbol)

Notes

The authors declare no competing financial interests.

ACKNOWLEDGMENT

This work was supported by the Department of Energy, Basic Energy Sciences, grant DE-FG02-03ER15483. ACT acknowledges the National Science Foundation for a graduate fellowship. SECCM, UV-Vis, and XPS data were collected at the Molecular Materials Research Center in the Beckman Institute of the California Institute of Technology. We gratefully acknowledge the critical support and infrastructure provided for this work by The Kavli Nanoscience Institute at Caltech.

REFERENCES

(1) Nielander, A. C.; Bierman, M. J.; Petrone, N.; Strandwitz, N. C.; Ardo, S.; Yang, F.; Hone, J.; Lewis, N. S., Photoelectrochemical Behavior of N-Type Si(111) Electrodes Coated with a Single Layer of Graphene. *J. Am. Chem. Soc.* **2013,** *135*, 17246-17249.

(2) Nielander, A. C.; Thompson, A. C.; Roske, C. W.; Maslyn, J. A.; Hao, Y.; Plymale, N. T.; Hone, J.; Lewis, N. S., Lightly Fluorinated Graphene As a Protective Layer for N-Type Si(111) Photoanodes in Aqueous Electrolytes. *Nano Lett.* **2016,** *16*, 4082-4086.

(3) Takahashi, T.; Tokailin, H.; Sagawa, T., Angle-Resolved Ultraviolet Photoelectron Spectroscopy of the Unoccupied Band Structure of Graphite. *Phys. Rev. B* **1985,** *32*, 8317-8324.

(4) Novoselov, K. S.; Geim, A. K.; Morozov, S. V.; Jiang, D.; Zhang, Y.; Dubonos, S. V.; Grigorieva, I. V.; Firsov, A. A., Electric Field Effect in Atomically Thin Carbon Films. *Science* **2004,** *306*, 666-669.

(5) Di Bartolomeo, A., Graphene Schottky Diodes: An Experimental Review of the Rectifying Graphene/Semiconductor Heterojunction. *Phys. Rep.* **2016,** *606*, 1-58.

(6) Lee, M.-H.; Cho, Y.; Byun, K.-E.; Shin, K. W.; Nam, S.-G.; Kim, C.; Kim, H.; Han, S.-A.; Kim, S.-W.; Shin, H.-J.; Park, S., Two-Dimensional Materials Inserted at the Metal/Semiconductor Interface: Attractive Candidates for Semiconductor Device Contacts. *Nano Lett.* **2018,** *18*, 4878-4884.

(7) Yoon, H. H.; Jung, S.; Choi, G.; Kim, J.; Jeon, Y.; Kim, Y. S.; Jeong, H. Y.; Kim, K.; Kwon, S.-Y.; Park, K., Strong Fermi-Level Pinning at Metal/N-Si(001) Interface Ensured by Forming an Intact Schottky Contact with a Graphene Insertion Layer. *Nano Lett.* **2017,** *17*, 44-49.

(8) Cassabois, G.; Valvin, P.; Gil, B., Hexagonal Boron Nitride Is an Indirect Bandgap Semiconductor. *Nat. Photonics* **2016,** *10*, 262-266.

(9) Chen, D.; Zhang, H.; Liu, Y.; Li, J., Graphene and Its Derivatives for the Development of Solar Cells, Photoelectrochemical, and Photocatalytic Applications. *Energ. Environ. Sci.* **2013,** *6*, 1362-1387.

(10) Britnell, L.; Gorbachev, R. V.; Jalil, R.; Belle, B. D.; Schedin, F.; Katsnelson, M. I.; Eaves, L.; Morozov, S. V.; Mayorov, A. S.; Peres, N. M. R.; Castro Neto, A. H.; Leist, J.; Geim, A. K.;

Ponomarenko, L. A.; Novoselov, K. S., Electron Tunneling through Ultrathin Boron Nitride Crystalline Barriers. *Nano Lett.* **2012,** *12*, 1707-1710.

(11) Meng, J.-H.; Liu, X.; Zhang, X.-W.; Zhang, Y.; Wang, H.-L.; Yin, Z.-G.; Zhang, Y.-Z.; Liu, H.; You, J.-B.; Yan, H., Interface Engineering for Highly Efficient Graphene-on-Silicon Schottky Junction Solar Cells by Introducing a Hexagonal Boron Nitride Interlayer. *Nano Energy* **2016,** *28*, 44-50.

(12) Byun, K.-E.; Chung, H.-J.; Lee, J.; Yang, H.; Song, H. J.; Heo, J.; Seo, D. H.; Park, S.; Hwang, S. W.; Yoo, I.; Kim, K., Graphene for True Ohmic Contact at Metal–Semiconductor Junctions. *Nano Lett.* **2013,** *13*, 4001-4005.

(13) Khomyakov, P. A.; Giovannetti, G.; Rusu, P. C.; Brocks, G.; van den Brink, J.; Kelly, P. J., First-Principles Study of the Interaction and Charge Transfer between Graphene and Metals. *Phys. Rev. B* **2009,** *79*, 195425.

(14) Bokdam, M.; Brocks, G.; Katsnelson, M. I.; Kelly, P. J., Schottky Barriers at Hexagonal Boron Nitride/Metal Interfaces: A First-Principles Study. *Phys. Rev. B* **2014,** *90*, 085415.

(15) Leong, W. S.; Luo, X.; Li, Y.; Khoo, K. H.; Quek, S. Y.; Thong, J. T. L., Low Resistance Metal Contacts to MoS_2 Devices with Nickel-Etched-Graphene Electrodes. *ACS Nano* **2015,** *9*, 869-877.

(16) Denis, P. A.; Iribarne, F., Comparative Study of Defect Reactivity in Graphene. *J. Phys. Chem. C* **2013,** *117*, 19048-19055.

(17) Ebejer, N.; Schnippering, M.; Colburn, A. W.; Edwards, M. A.; Unwin, P. R., Localized High Resolution Electrochemistry and Multifunctional Imaging: Scanning Electrochemical Cell Microscopy. *Anal. Chem.* **2010,** *82*, 9141-9145.

(18) Snowden, M. E.; Güell, A. G.; Lai, S. C. S.; McKelvey, K.; Ebejer, N.; O'Connell, M. A.; Colburn, A. W.; Unwin, P. R., Scanning Electrochemical Cell Microscopy: Theory and Experiment for Quantitative High Resolution Spatially-Resolved Voltammetry and Simultaneous Ion-Conductance Measurements. *Anal. Chem.* **2012,** *84*, 2483-2491.

(19) Güell, A. G.; Cuharuc, A. S.; Kim, Y.-R.; Zhang, G.; Tan, S.-y.; Ebejer, N.; Unwin, P. R., Redox-Dependent Spatially Resolved Electrochemistry at Graphene and Graphite Step Edges. *ACS Nano* **2015,** *9*, 3558-3571.

(20) Aaronson, B. D. B.; Byers, J. C.; Colburn, A. W.; McKelvey, K.; Unwin, P. R., Scanning Electrochemical Cell Microscopy Platform for Ultrasensitive Photoelectrochemical Imaging. *Anal. Chem.* **2015,** *87*, 4129-4133.

(21) Chen, R.; Nioradze, N.; Santhosh, P.; Li, Z.; Surwade, S. P.; Shenoy, G. J.; Parobek, D. G.; Kim, M. A.; Liu, H.; Amemiya, S., Ultrafast Electron Transfer Kinetics of Graphene Grown by Chemical Vapor Deposition. *Angew. Chem. Int. Ed.* **2015,** *54*, 15134-15137.

(22) Tan, C.; Rodríguez-López, J.; Parks, J. J.; Ritzert, N. L.; Ralph, D. C.; Abruña, H. D., Reactivity of Monolayer Chemical Vapor Deposited Graphene Imperfections Studied Using Scanning Electrochemical Microscopy. *ACS Nano* **2012,** *6*, 3070-3079.

(23) Todt, M. A.; Isenberg, A. E.; Nanayakkara, S. U.; Miller, E. M.; Sambur, J. B., Single-Nanoflake Photo-Electrochemistry Reveals Champion and Spectator Flakes in Exfoliated $MoSe_2$ Films. *J. Phys. Chem. C* **2018,** *122*, 6539-6545.

(24) Ghilane, J.; Hapiot, P.; Bard, A. J., Metal/Polypyrrole Quasi-Reference Electrode for Voltammetry in Nonaqueous and Aqueous Solutions. *Anal. Chem.* **2006,** *78*, 6868-6872.

(25) Kim, J.; Shen, M.; Nioradze, N.; Amemiya, S., Stabilizing Nanometer Scale Tip-to-Substrate Gaps in Scanning Electrochemical Microscopy Using an Isothermal Chamber for Thermal Drift Suppression. *Anal. Chem.* **2012,** *84*, 3489-3492.

(26) Li, X.; Zhu, Y.; Cai, W.; Borysiak, M.; Han, B.; Chen, D.; Piner, R. D.; Colombo, L.; Ruoff, R. S., Transfer of Large-Area Graphene Films for High-Performance Transparent Conductive Electrodes. *Nano Lett.* **2009,** *9*, 4359-4363.

(27) Pirkle, A.; Chan, J.; Venugopal, A.; Hinojos, D.; Magnuson, C. W.; McDonnell, S.; Colombo, L.; Vogel, E. M.; Ruoff, R. S.; Wallace, R. M., The Effect of Chemical Residues on the Physical and Electrical Properties of Chemical Vapor Deposited Graphene Transferred to SiO_2. *Appl. Phys. Lett.* **2011,** *99*, 122108.

(28) Suk, J. W.; Kitt, A.; Magnuson, C. W.; Hao, Y.; Ahmed, S.; An, J.; Swan, A. K.; Goldberg, B. B.; Ruoff, R. S., Transfer of CVD-grown Monolayer Graphene onto Arbitrary Substrates. *ACS Nano* **2011,** *5*, 6916-6924.

(29) Bentley, C. L.; Kang, M.; Unwin, P. R., Nanoscale Structure Dynamics within Electrocatalytic Materials. *J. Am. Chem. Soc.* **2017,** *139*, 16813-16821.

(30) Bentley, C. L.; Kang, M.; Maddar, F. M.; Li, F.; Walker, M.; Zhang, J.; Unwin, P. R., Electrochemical Maps and Movies of the Hydrogen Evolution Reaction on Natural Crystals of Molybdenite (MoS_2): Basal Vs. Edge Plane Activity. *Chem. Sci.* **2017,** *8*, 6583-6593.

(31) Grimm, R. L.; Bierman, M. J.; O'Leary, L. E.; Strandwitz, N. C.; Brunschwig, B. S.; Lewis, N. S., Comparison of the Photoelectrochemical Behavior of H-Terminated and Methyl-terminated Si(111) Surfaces in Contact with a Series of One-Electron, Outer-Sphere Redox Couples in CH_3CN. *J. Phys. Chem. C* **2012,** *116*, 23569-23576.

(32) Lewis, N. S., A Quantitative Investigation of the Open-Circuit Photovoltage at the Semiconductor/Liquid Interface. *J. Electrochem. Soc.* **1984,** *131*, 2496-2503.

(33) Banhart, F.; Kotakoski, J.; Krasheninnikov, A. V., Structural Defects in Graphene. *ACS Nano* **2011,** *5*, 26-41.

(34) Serpone, N.; Pelizzetti, E., *Photocatalysis : Fundamentals and Applications*. Wiley: New York, 1989.

(35) Gleason-Rohrer, D. C.; Brunschwig, B. S.; Lewis, N. S., Measurement of the Band Bending and Surface Dipole at Chemically Functionalized Si(111)/Vacuum Interfaces. *J. Phys. Chem. C* **2013,** *117*, 18031-18042.

(36) Lányi, Š.; Nádaždy, V., Scanning Probe Microscope Based Deep-Level Spectroscopy of Semiconductor Films. *Ultramicroscopy* **2010,** *110*, 655-658.

(37) Doan, Q. T.; El Hdiy, A.; Troyon, M., Three-Dimensional Simulation of Electron Beam Induced Current Collected by a Nano-Contact: Diffusion and Collection Analysis. *J. Appl. Phys.* **2011,** *110*, 124515.

(38) Doan, Q.-T.; Hamdouni, A.; El Hdiy, A., Surface Recombination Velocity Effects on Simulated Electron Beam Induced Current Collected by a Nanoscale Electrode. *Superlattice Microst.* **2016,** *100*, 1296-1300.

(39) Marchiando, J. F.; Kopanski, J. J.; Lowney, J. R., Model Database for Determining Dopant Profiles from Scanning Capacitance Microscope Measurements. *J. Vac. Sci. Technol. B* **1998,** *16*, 463-470.

(40) Marchiando, J. F.; Kopanski, J. J.; Albers, J., Limitations of the Calibration Curve Method for Determining Dopant Profiles from Scanning Capacitance Microscope Measurements. *J. Vac. Sci. Technol. B* **2000,** *18*, 414-417.

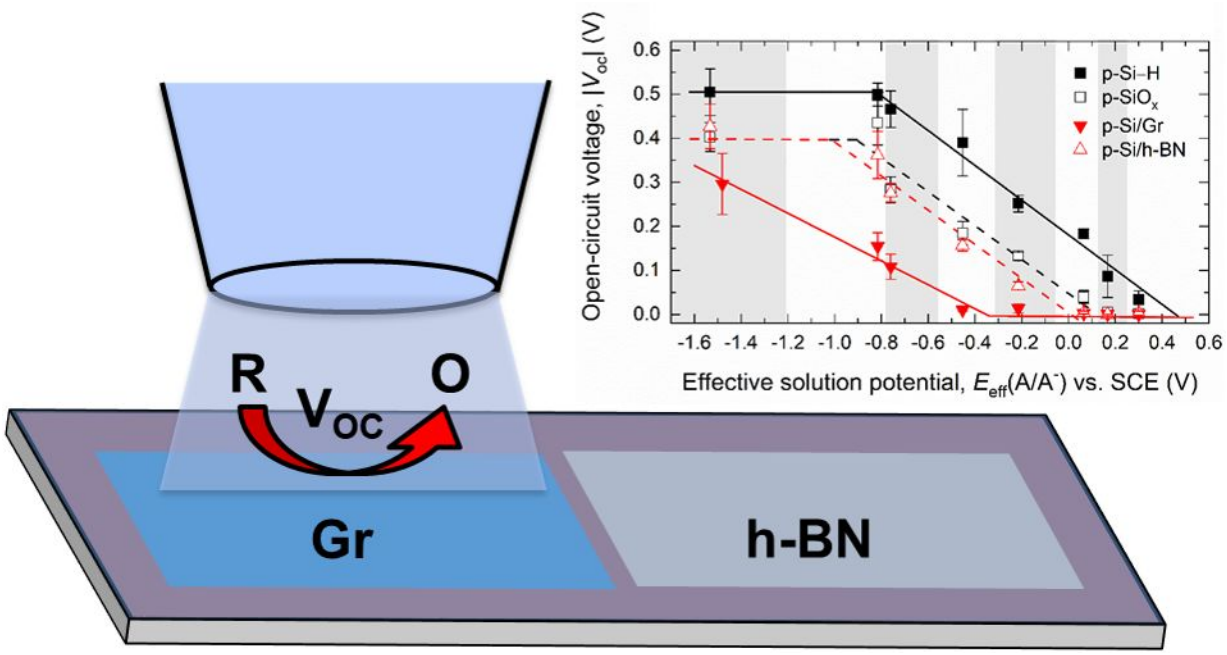
R
O
V_{OC}
Gr
h-BN
Open-circuit voltage, $|V_{ocl}|$ (V)
0.6
0.5
0.4
0.3
0.2
0.1
0.0
-1.6 -1.4 -1.2 -1.0 -0.8 -0.6 -0.4 -0.2 0.0 0.2 0.4 0.6
Effective solution potential, E_{eff}(A/A$^-$) vs. SCE (V)
p-Si–H
p-SiO$_x$
p-Si/Gr
p-Si/h-BN

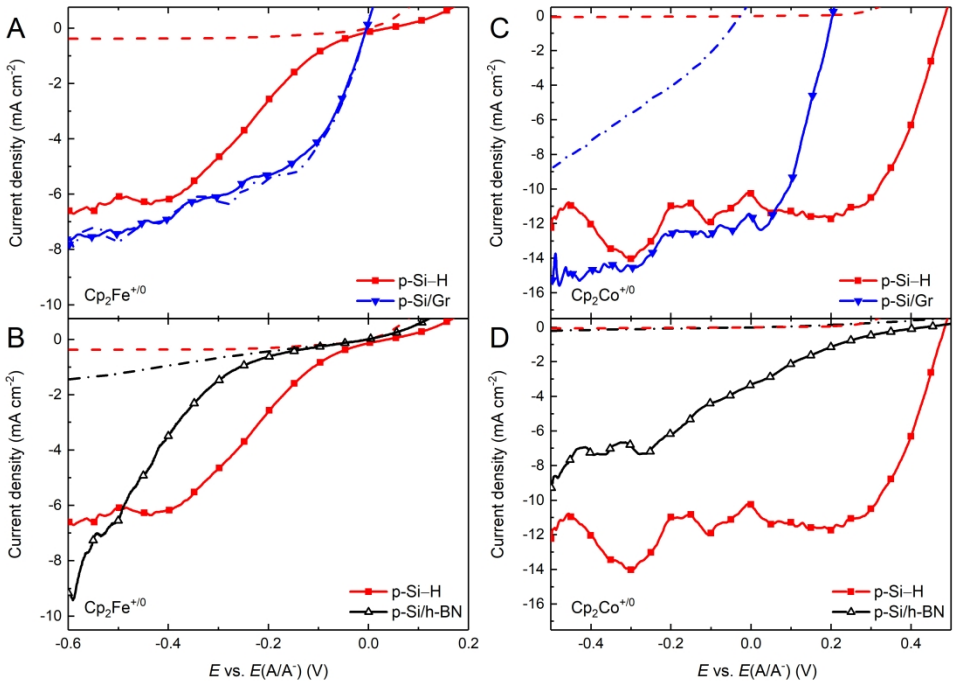

Photocurrent density vs potential (*J*-*E*) behavior of modified p-Si electrodes in contact with $Cp_2Fe^{+/0}$ (A-B) and $Cp_2Co^{+/0}$ (C-D), in CH_3CN–0.50 M $LiClO_4$ under 100 mW cm^{-2} of ELH-type simulated solar illumination. The dashed lines show scans of the same electrodes without illumination. In contact with either redox couple, the fill factor of the p-Si/h-BN electrode was substantially smaller than that of either the p-Si–H (Figure 1) or p-SiO_x (Figure S7) electrodes, indicative of slow electron-transfer kinetics at the h-BN/liquid interface. In contact with $Cp_2Co^{+/0}$, the *J*-*E* characteristics of the p-Si/Gr electrode shifted upon illumination, in addition to displaying substantially larger reverse saturation current densities than the other three types of electrodes.

177x128mm (600 x 600 DPI)

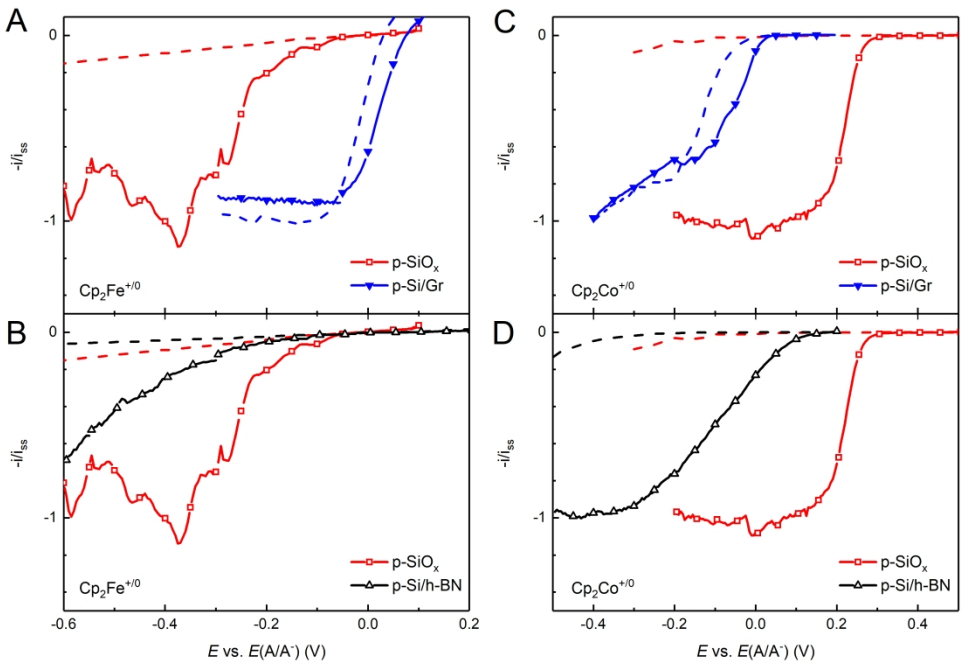

Photocurrent vs potential (*I-E*) behavior in contact with CH_3CN–0.50 M $LiClO_4$ under 100 mW cm^{-2} of ELH-type simulated solar illumination determined by SECCM for p-Si electrodes in contact with $Cp_2Fe^{+/0}$ (A-B) and $Cp_2Co^{+/0}$ (C-D). The dashed lines show scans of the same electrodes without illumination. The data in SECCM measurements were similar to data observed in the macroscale measurements (Figure 1). Si–H surfaces were not probed by SECCM because the O_2 and water content in the flush box used for these experiments resulted in the formation of oxide on freshly etched Si–H samples more rapidly than measurements could be performed.

177x125mm (600 x 600 DPI)

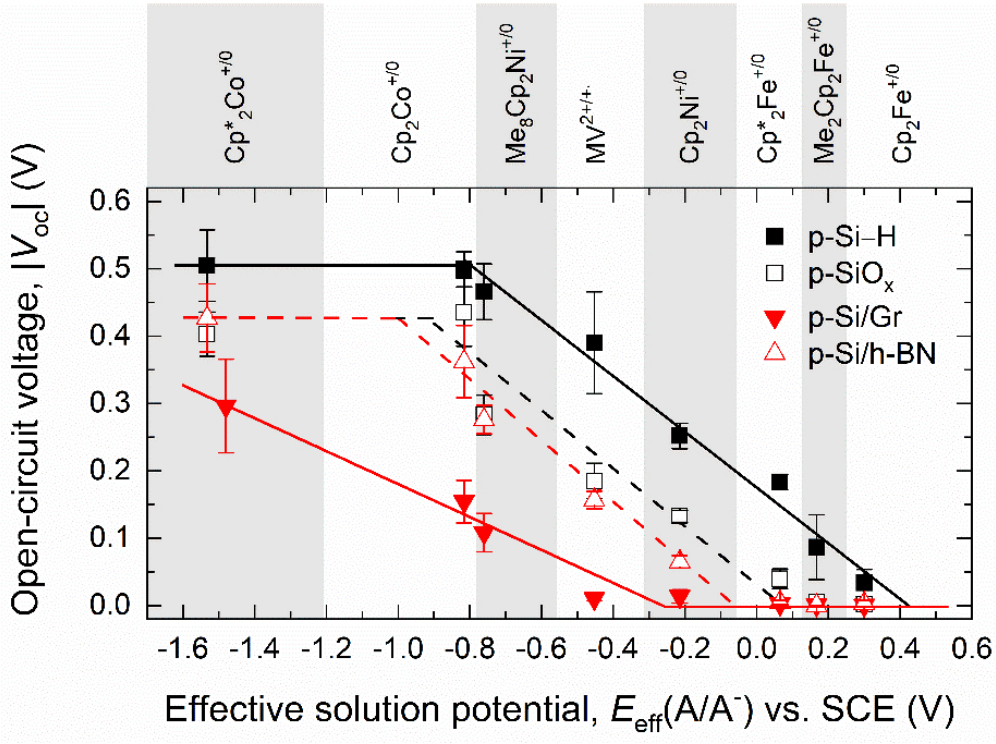

Comparison of open-circuit voltage of macroscale p-Si–H, p-SiO_x, p-Si/Gr, and p-Si/h-BN electrodes, respectively, versus the effective redox potential of various redox couples. Three regions, each highlighted by linear fits of the data therein, were identified for all samples.

105x78mm (220 x 220 DPI)

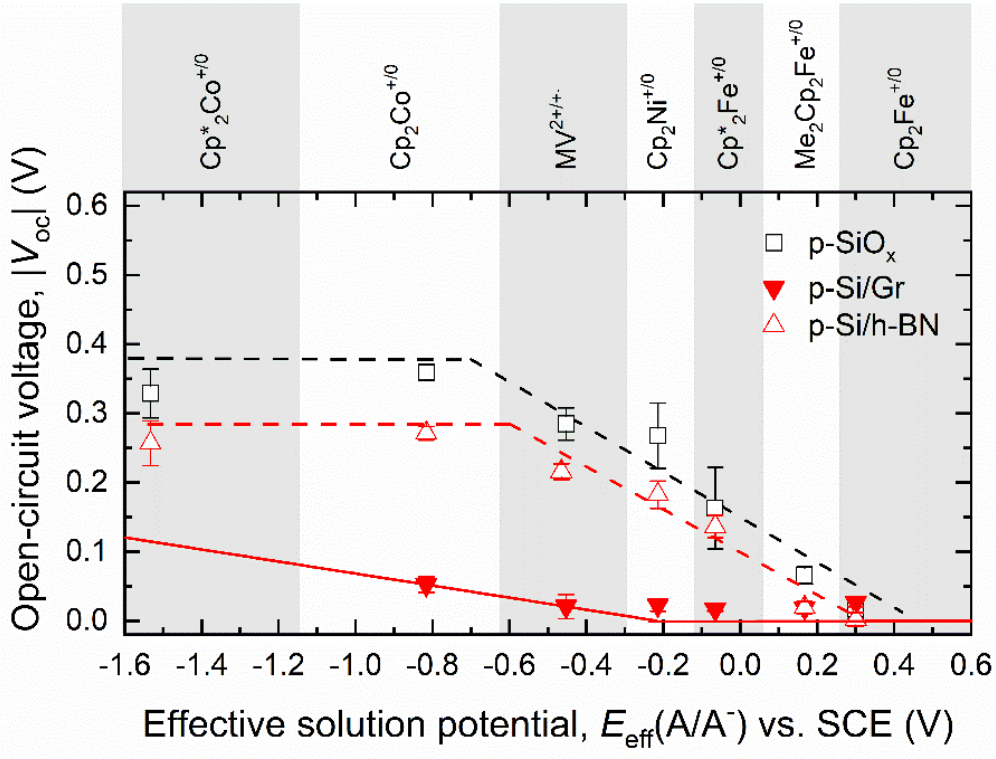

Comparison of the open-circuit voltage of p-SiO_x, p-Si/Gr, and p-Si/h-BN electrodes, respectively, versus the effective potential of various redox couples, on the same SECCM electrode. Linear fits of the data have been used to highlight the different regions of behavior.

103x78mm (220 x 220 DPI)

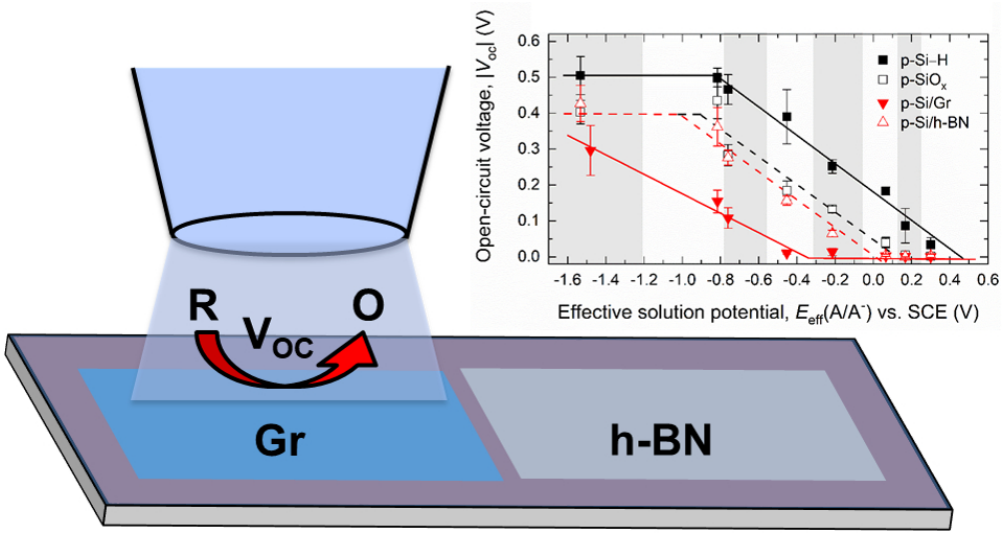

Table Of Contents Figure

161x86mm (150 x 150 DPI)